International Journal of Pharmaceutics: X 8 (2024) 100282

Contents lists available at ScienceDirect

International Journal of Pharmaceutics: X

journal homepage: www.sciencedirect.com/journal/international-journal-of-pharmaceutics-x

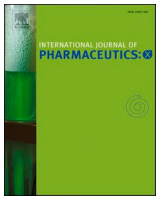

A simple nanoplatform of thermo-sensitive liposomes and gold nanorods to treat bone metastasis through improved chemotherapy combined with photothermal therapy

Jia Gu [a,b], Lifan Jiang [a], Zhongping Chen [b,*], Jun Qi [a,*]

[a] Department of Burns and Plastic Surgery, Affiliated Hospital of Nantong University, Nantong, People's Republic of China
[b] Institute of Special Environmental Medicine, Nantong University, Nantong, People's Republic of China

ARTICLE INFO

Keywords:
Liposomes
Sensitive release
Gold nanorods
Photothermal therapy
Bone metastasis

ABSTRACT

Bone metastasis remains a clinical challenge and is still considered incurable. While nanoparticles-based drug delivery and photothermal therapy (PTT) show promise in treating subcutaneous solid tumor, their therapeutic outcome in treating bone metastasis is limited, due to the inaccessibility of bone metastatic site and the complexity of bone metastasis. Herein, we reported a simple nanoplatform composed of thermo-sensitive liposomes (TSL) and gold nanorods (GNR) to treat bone metastasis through improved chemotherapy combined with GNR-assisted PTT. Lipid combination of TSL was firstly tailored to regulate its stability under physiological condition as well as its sensitivity in responding to PTT-caused mild hyperthermia. The obtained TSL with loaded drug was then combined with GNR to form the nanoplatform through unsophisticated incubation. Cell experiments revealed that upon near-infrared (NIR) irradiation, the nanoplatform effectively inhibited the viability and migration ability of tumor cells through PTT, PTT-triggered thermo-sensitive drug release, and PTT-augmented sensitivity of tumor cells to drug. In a murine model of bone metastasis, the nanoplatform enabled effective delivery of loaded drug and GNR to bone metastatic site for rapid drug release upon local NIR irradiation. Through killing tumor cells and rebalancing the turnover of osteoclasts and osteoblasts, the nanoplatform largely preserved bone structure for pain relief and survival extension. Inspired by the simplicity of nanoplatform acquirement and treatment operation, the strategy of liposomes-based thermo-sensitive drug delivery in combination with GNR-assisted PTT is considered greatly promising in treating bone metastasis.

1. Introduction

Bone is a common site for cancer metastasis, ranking after the liver and lung (Hu et al., 2022). Bone metastasis has a high morbidity and mortality. Approximately 70–80 % of patients with advanced breast and prostate cancers, and more than 30 % of patients with thyroid, lung, kidney, and bladder cancers will ultimately develop bone metastasis, which accounts for 15–20 % of total metastases (Gao et al., 2021; Weilbaecher et al., 2011). While regional and localized cancer is not lethal, bone metastasis remains a clinical challenge and is currently considered incurable. Once metastasizing to the bone, the 5-year survival rate of cancer patients sharply decreases to 1 % for lung cancer, 6 % for prostate cancer, and 13 % for breast cancer with the median survival time less than one year (Svensson et al., 2017). Moreover, bone metastasis is always accompanied with skeletal-related events including skeletal pain, pathological fracture, hypercalcemia, and spinal cord compression, which remarkably reduce quality of life and further worsen survival.

Preoperative or postoperative chemotherapy is the standard treatment for bone metastasis and however, still suffers from poor therapeutic outcome. The reasons are multiple. Firstly, different from soft tissues, bone as a hard tissue is rigid with low permeability and reduced blood flow, which hinders the achievement of sufficient dose through systemic medication. Secondly, to reach therapeutic window, high-dose dosing is needed and consequent unfavorable side effect will result in poor prognosis. Thirdly, unique bone microenvironment provides a protective effect against chemotherapy. In-depth understanding of basic biology of bone metastasis drives the development of advanced therapies such as hormone therapy, immunotherapy, and anti-resorptive therapy (Yu et al., 2023). However, these treatments are usually

* Corresponding authors.
E-mail addresses: chenzp@ntu.edu.cn (Z. Chen), qijunsky@126.com (J. Qi).

https://doi.org/10.1016/j.ijpx.2024.100282
Received 26 June 2024; Received in revised form 26 August 2024; Accepted 29 August 2024
Available online 30 August 2024

palliative with only modest clinical outcome in enhancing survival. For example, bisphosphonate-based anti-resorptive therapy can delay the development of skeletal-related events as well as decreasing pain in a short term, and unfortunately, shows no statistical significance in the overall survival and progression-free survival when compared with placebo (Lorange et al., 2023). Following anti-resorptive therapy, up to 50 % of patients will even develop new bone metastases (Roodman, 2004).

Nanoparticles-based drug delivery systems (NDDSs) provide a new therapeutic avenue for bone metastasis (Fan et al., 2024; Liu et al., 2023a). While reducing side effects by shielding chemotherapeutic drugs, NDDSs can improve pharmacokinetics of free drugs and facilitate their accumulation at tumor site through the enhanced permeability and retention (EPR) effects to benefit therapeutic outcome. To further enhance drug accumulation and drug bioavailability at bone metastatic site for maximizing therapeutic outcome, NDDSs can be further decorated for targeted delivery by targeting tumor, bone, and bone microenvironment (Li et al., 2024), and/or stimuli-sensitive delivery capable of responding to exogenous stimuli such as light and heart, and/or endogenous stimuli from bone microenvironment such as acidic pH, high redox potential, and hypoxia (Lavrador et al., 2018; Long et al., 2021). A great number of targeted and/or sensitive NDDSs with improved therapeutic outcome in inhibiting bone metastasis and its caused pain have been extensively reported (Li et al., 2023; Ren et al., 2022). However, due to the inaccessibility of bone metastatic site and the complexity of bone metastasis, these smart NDDSs-based chemotherapy strategy even using combination of several chemotherapeutic drugs for bone metastasis are still limited to some extent. Given that combinational therapy is more effective than single chemotherapy, attempts are continuously made to develop new treatment modalities. Photothermal therapy (PTT) can kill tumor through light-heat conversion of photothermal agents for local hyperthermia, while exerting few side effects to normal tissues. Moreover, local hyperthermia can increase the sensitivity of tumor cells to chemotherapeutic drugs and thus promote the efficiency of chemotherapy (Sheng et al., 2023; Tang et al., 2024). Together with its minimal invasiveness, time-spatial controllability, and simplicity of operation, PTT has been evidenced as an effective and safe treatment modality (Guo et al., 2018; Roy et al., 2023). However, despite great success in solid tumor ablation, the application of PTT alone in deep and internal bone metastasis is severely hampered, probably as a result of thermal resistance, limited irradiation area, and insufficient bone penetration depth (Chao et al., 2023). Therefore, multifunctional nanoplatform combining currently available systemic therapies with adjuvant PTT emerges as a prospective alternative to promote therapeutic outcome (Amiryaghoubi et al., 2023; Ashique et al., 2023).

Among versatile nanoplatforms for combinational therapy, the nanoplatform employing thermo-sensitive NDDSs and photothermal agents for photothermo-chemotherapy gains more attentions, due to its relatively high synergistic effect by thermal ablation of cancer cells and thermo-sensitive anti-tumor drug release. Instead of sophisticated structure design and chemical modification (Chen et al., 2024; Gautam et al., 2024), we herein report an easily achievable nanoplatform employing highly thermo-sensitive TSL as carrier of doxorubicin (DOX) and GNR as photothermal agent to treat bone metastasis. The nanoplatform was formed by simple incubation of TSL and GNR and was then intravenously injected. After local irradiation with NIR laser of 808 nm at bone metastatic site, the synergistic therapeutic outcome in bone metastasis inhibition and pain relief is evaluated.

2. Materials and methods

2.1. Materials

The lipids including 1,2-dipalmitoyl-sn-glycero-3-phosphorylcholine (DPPC), 1,2-dimyristoyl-sn-glycero-3-phosphocholine (DMPC), 1,2-distearoyl-sn-glycero-3-phosphoethanolamine-poly(ethylene glycol) with terminated thiol (DSPE-PEG-SH), and cholesterol (Chol) were purchased from AVT (Shanghai) Pharmaceutical Tech Co., Ltd. (Shanghai, China). Hydrophilic doxorubicin hydrochloride (DOX) was purchased from Meryer Co. Ltd. (Shanghai, China). 3-(4,5)-dimethylthiahiazo(−z-y1)-3,5-di-phenytetrazoliumromide (MTT) was purchased from Sigma-Aldrich (MO, USA). The other main chemicals were from Sinopharm Chemical Reagent Co. Ltd. (Shanghai, China). Fetal bovine serum (FBS) was purchased from Gibco Life Technologies (AG, Switzerland). Dulbecco's Modified Eagle's Medium (DMEM) was from Invitrogen Corporation (CA, USA). All chemicals were analytical or HPLC grade and used as received.

Mouse prostate cancer cells (RM-1) line was obtained from Institute of Biochemistry and Cell Biology, Chinese Academy of Sciences (Shanghai, China). Nanoparticles synthesis.

2.1.1. Synthesis of GNR

GNR was a gift from Dr. Zhirui Guo from the Second Affiliated Hospital of Nanjing Medical University. The synthetic procedures have been detailed in their work (Liu et al., 2011; Zhang et al., 2021). GNR was quantified in an inductively coupled plasma optical emission spectrometer (ICP-OES, Agilent 5100).

2.2. Synthesis of DOX loaded TSL (DOX-TSL)

TSL were synthesized according to the protocol well established our previous work (Cao et al., 2019; Long et al., 2020; Tao and Chen, 2024). Blank TSL were formulated with (67-X)% DPPC, X% DMPC, 30 % Chol, and 3 % DSPE-PEG-SH (molar ratio, X% = 4, 8, 16, and 32 %). Briefly, all lipids were dissolved in chloroform in a round-bottomed flask and then dried to form a thin film through rotary evaporation in water bath at 60 °C. The resulting film was left overnight to completely remove chloroform and then hydrated with 250 mM citric acid solution, followed by sonication at 45 °C. After dialysis against PBS (pH = 7.4), blank TSL with transmembrane pH gradient was obtained. To load DOX, DOX was added to blank TSL suspension at 1:5 (weight ratio) and the mixture was incubated at 60 °C for 40 min to produce DOX-TSL suspension.

2.3. Nanoparticles characterization

2.3.1. Morphology, size, polydispersity, and zeta potential

The morphology and size of TSL and GNR were observed on a transmission electron microscope (TEM, JEM-1230, Japan). The hydrodynamic diameter, polydispersity (PDI), and zeta potential of TSL were determined by dynamic light scattering (DLS, Zetasizer ZS90, Malvern). DLS measurements were carried out at least in triplicate.

2.3.2. Differential scanning calorimetry (DSC)

DSC thermograms were obtained on DSC 8000 (PerkinElmer, USA). The measurement started at 16 °C and the temperature was raised at a rate of 1 °C/min to 60 °C.

2.3.3. Drug loading and in vitro drug release of TSL

DOX loading and *in vitro* DOX release were determined on a high-performance liquid chromatography (HPLC, Waters) system equipped with a fluorescence detector (2475 FLR Detector) with the HPLC conditions detailed in our previous work (Long et al., 2021). To determine DOX entrapment efficiency (EE%), the prepared DOX-TSL suspension was centrifuged at 12000 rpm for 10 min and the supernatant containing unloaded DOX was collected for HPLC analysis. EE% was defined as loaded DOX normalized to totally added DOX.

To determine *in vitro* drug release for evaluating stability and thermo-sensitivity of TSL, the prepared DOX-TSL suspension was transferred into a dialysis bag and dialyzed against PBS (pH = 7.4) at 25 °C (room temperature), 37 °C (physiological temperature), and 37 °C

for 12 h plus 43 °C for 10 min and 37 °C for remaining time (PTT treatment condition), respectively. The dialysis lasted for 24 h and at the predetermined timepoints (12 h and 24 h), aliquots of the dialysate containing released DOX was withdrawn for HPLC analysis.

2.3.4. Photothermal property of GNR

Ultraviolet-visible (UV–Vis) spectrum of GNR was recorded on an UV-3600 spectrophotometer (Shimadzu, Japan). The effects of GNR concentration and NIR power on the photothermal properties of GNR were investigated. Aqueous GNR solutions with varied concentrations (50, 100, 200, and 400 μg/mL) were placed in a 1.5 mL Eppendorf tube (1 mL solution of each sample) and exposed to an 808 nm NIR laser at different powers (0.5, 1.0, and 2.0 W/cm^2, Changchun New Industries Optoelectronics Technology, China) for 10 min. At the same point of GNR solution, the temperature was recorded every 2 min using a temperature probe (YZ-1650, Yangzi, China).

2.4. Cell experiments

2.4.1. Cell culture

RM-1 cells were cultured in DMEM supplemented with 10 % fetal bovine serum (FBS) in a humidified atmosphere containing 5 % CO_2.

2.4.2. Cytotoxicity and cell migration

In vitro cytotoxicity of GNR, DOX, DOX-TSL, and the nanoplatform of DOX-TSL and GNR (DOX-TSL + GNR) with or without NIR irradiation was first assessed by MTT. The nanoplatform was formed by simply incubating pre-synthesized DOX-TSL and GNR with gentle shaking for 30 min, allowing for potential conjugation of DOX-TSL and GNR through gold-thiol of lipid-PEG coupling. RM-1 cells seeded in 96-well plate with a density of 3000 cells per well were incubated with GNR (25, 50, 100, 200, and 400 μg/mL), DOX, DOX-TSL (0.2, 0.4, 0.8, and 1.6 μg/mL), and the nanoplatform, respectively, for 3 h. The cells were then washed with fresh media followed by incubation for another 21 h. Finally, the cells were treated for MTT on a microplate reader (Synergy 2, BioTek). Similarly, RM-1 cells were treated for Calcein-AM/PI double staining to detect living/dead cells according to the standard protocol recommended by the manufacturer.

Cell migration was assessed by wound healing assay. RM-1 cells were seeded in 6-well plate (20,000 cells per well) and then treated with DOX, GNR, and DOX-TSL + GNR at 1.0 μg/mL of DOX and 100 μg/mL of GNR for 3 h. After washing, a wound area was generated using a 10 μL pipette tip to scrap cell monolayer. The cells were further incubated for 21 h and the wound width was observed on an inverted microscope to calculate migration ratio. Migration ratio was defined as reduced area relative to initial wound area acquired by Image J software.

In the case of NIR irradiation, cells were irradiated for 5 min at the power of 0.5 W/cm^2 before further incubation for 21 h.

2.4.3. Cellular uptake and intracellular drug release

RM-1 cells treated with DOX and DOX-TSL + GNR at 0.4 μg/mL of DOX and 100 μg/mL of GNR for 3 h. The cells were then incubated in fresh media and at the predetermined intervals (0, 1, 2, and 4 h) with or without NIR irradiation, the cells were washed and fixed with 4 % paraformaldehyde for DOX fluorescence observation using a confocal laser scanning microscope (CLSM, TCS SP8, Leica) to study cellular uptake and intracellular drug release of TSL. A fluorescent filter of 488 laser and 590 ± 20 nm emission was utilized for DOX. In the case of NIR irradiation, cells were irradiated for 5 min at the power of 0.5 W/cm^2.

2.5. Animal experiments

2.5.1. Animal model of bone metastasis

C57BL/6 mice (aged 8–10 weeks, 18–22 g in body weight, male) were obtained from Animal Center of Nantong University. All animal studies were approved by the Animal Care and Use Committee of Nantong University (Approval ID: P20230301–025) and the Jiangsu Province Animal Care Ethics Committee (Approval ID: SYXK[SU] 2007–0021).

A murine model of bone metastasis was established by directly injecting RM-1 cells into the tibia of hind limb of C57BL/6 mice, which was described in detail in our previous work (Long et al., 2021; Wang et al., 2014). The mice were housed in standard cages and given free access to food and water. It was noted that animal experimenters were blinded to the treatment while processing data.

2.5.2. Tissue distribution and NIR imaging

Tissue distribution was assessed in tumor-bearing C57BL/6 mice. On the 7th day after tumor modeling, randomly grouped mice intravenously received drug treatment of DOX, DOX-TSL, and the nanoplatform at 5 mg/kg body weight of DOX and 10 mg/kg body weight of GNR (n = 3, 9 mice in total). At 12 h post-injection, all mice were euthanized through cervical dislocation to harvest some tissues of the heart, liver, spleen, lung, kidney, tumor-free bone, and tumor-bearing bone. Tissue samples were mixed with 1 % SDS (0.1 mL/5 mg tissue) and then vigorously smashed using a homogenizer (FastPrep-24TM 5G, Boyi Biotech, China). After removing crumbling tissues, the samples were prepared for studying tissue distribution. To determine DOX content, the samples were mixed with acetonitrile (1:3, *v*/v) to extract DOX for HPLC analysis. Extracted DOX needed filtering with a syringe filter (0.45 μm in pore diameter) to completely remove protein for HPLC analysis. To determine GNR content, the samples were treated with aqua regia (1:2, v/v) for ICP-OES analysis. After 24 h treatment, aqua regia was removed through heating and then diluted for the analysis.

Meanwhile, NIR imaging was carried out to study intratumoral DOX release upon NIR irradiation. On the 7th day after tumor modeling, mice intravenously received drug treatment of the nanoplatform at 5 mg/kg body weight of DOX and 10 mg/kg body weight of GNR (6 mice in total). At 12 h post-injection, bone metastatic site of 3 mice was irradiated for 10 min at the power of 0.5 W/cm^2. Immediately afterwards, all mice were euthanized and some tissues of the heart, liver, spleen, lung, kidney, tumor-free bone, and tumor-bearing bone were harvested for *ex vivo* NIR imaging using a small animal dedicated IVIS imaging system (Lumina II, Caliper Life Sciences). DOX Fluorescence intensity was analyzed by IVIS imaging software.

2.5.3. Drug treatment, pain behavior test, and therapeutic evaluation

On the 7th day after tumor modeling, mice were randomly grouped as PBS, DOX, DOX-TSL, and DOX-TSL + GNR + NIR (n = 8, 32 mice in total), receiving intravenous treatment at 5 mg/kg body weight of DOX and 10 mg/kg body weight of GNR every four days for total three times. In the case of NIR irradiation, bone metastatic site of mice was irradiated for 10 min at the power of 0.5 W/cm^2 at 12 h post-injection.

On the 6th and 17th days, mechanical allodynia and thermal hyperalgesia of mice were tested to evaluate cancer-induced bone pain (CIBP). Mechanical allodynia was examined by measuring withdrawal responses of hind paw to a series of von Frey filaments with various strengths (Dixon, 1980). Thermal hyperalgesia was examined by measuring withdrawal latency of hind paw upon heat generated by a radiant beam (Hargreaves et al., 1988). Detailed protocols were described in our recent work (Huang et al., 2024).

The survival of mice was checked every day and all living mice were euthanized on the 35th day.

2.5.4. X-ray and computed tomography (CT) and assessments

In another animal experiment, tumor-bearing mice were grouped and treated with the same protocol described in Section 2.5.3 (n = 3, 12 mice in total). On the 20th day after tumor modeling, whole-body X-ray and CT assessments were performed on a clinical digital radiography (uDR 566i, United Imaging) and a clinical 16-slice CT scanner (Somatom Emotion, Siemens) and, respectively, to directly observe bone situation.

2.5.5. Bone staining

Following X-ray and CT assessments, hematoxylin and eosin (H&E) as well as tartrate-resistant acid phosphatase (TRAP) and alkaline phosphatase (ALP) (TRAP/ALP) staining of tumor-bearing bone as well as tumor-free bone were performed to obtain more bone information. Bone was decalcified and then cut into 6 μm slice for H&E staining or TRAP/ALP staining using TRAP/ALP staining kit® (Wako, Osaka, Japan). Detailed decalcification process was described in our previous work (Long et al., 2021).

Meanwhile, H&E staining of the heart, liver, spleen, lung, and kidney was performed to evaluate biosafety.

2.6. Data analysis

Data were statistically analyzed using unpaired student's *t*-test for two groups or one-way analysis of variance (ANOVA) test for multiple groups. A *p*-value less than 0.05 ($p < 0.05$) was considered significantly different.

3. Results and discussion

3.1. Synthesis and characterization of the nanoplatform

In this work, liposomes were chosen as thermo-sensitive NDDSs, due to their advantages: 1) they are safe and efficacious, verified by the fact that 80 % of approved cancer NDDSs are liposomes; 2) their stability under normal physiological conditions as well as response sensitivity to heat can be accurately tailored using marketed lipids being of different phase-transition temperatures; 3) they are easily surface-functionalized using polyethylene glycol (PEG)-lipid; 4) their synthetic procedure and effective loading of chemotherapeutic agent have been well established (Thapa and Kim, 2023). On the other hand, GNR was selected as photothermal agent, owing to its following features: 1) it has good NIR light-adsorbing ability for deep tissue penetration and excellent photothermal conversion efficiency; 2) compared with other photothermal nanomaterials with complicate structure or morphology for efficient photothermal conversion, its synthetic protocol has been well established; 3) it can easily connect with TSL for the formation of the nanoplatform through gold-thiol coupling between GNR and thiol-functionalized lipid in TSL (Taylor et al., 2022).

TSL, formulated with DPPC, DMPC, Chol, and DSPE-PEG-SH, was synthesized through thin film evaporation-hydration method, DMPC of which was additionally included to tailor the thermo-sensitivity of TSL. DOX was actively loaded, achieving a high EE% (Table S1). Fig. 1A showed the representative TEM image of DOX-TSL formulated with 63 % DPPC, 4 % DMPC, 30 % Chol, and 3 % DSPE-PEG-SH, which had spherical morphology with the diameter less than 80 nm. DPPC with the phase-transition temperature at 41 °C is widely used to fabricate TSL, whose thermo-sensitivity is unfortunately unsatisfactory. As shown in Table S2, TSL without DMPC could maintain its payload, releasing 24.8 % at room temperature and 35.1 % at the physiological temperature within 24 h. Under PTT treatment condition (37 °C for 12 h plus 43 °C for 10 min and returning to 37 °C for another 12 h, 24 h in total), the release was accelerated, which was, unfortunately, only 61 %. Inclusion of DMPC with the phase-transition temperature at 24 °C did not impair the stability of TSL, whereas endowing TSL with high thermo-sensitivity. However, the inclusive amount of DMPC was not positively correlated with the thermo-sensitivity, which was probably due to the interaction of DMPC with the other lipids as well as resultant lipid rearrangement of lipid bilayer. DSC results revealed that the phase-transition temperatures of TSL without DPPC and containing 4 % DMPC were around 55 °C and 50 °C, respectively (Fig. S1 and S2). As they could still sensitively respond to 43 °C for rapid drug release, this result strongly suggested that thermo-sensitive release of TSL was not merely determined by the phase-transition temperatures of TSL. Some other mechanisms are also involved. Generally, it was found that the TSL containing 4 % DMPC had comparable stability and considerably improved thermo-sensitivity compared with the other formulations (Fig. 1B), which was therefore selected as the formulation.

On the other hand, GNR was synthesized through seed-mediated growth. TEM image exhibited that the length of GNR was about 50 nm and its aspect ratio was around 4.0 (Fig. 1C). UV–vis spectrum of GNR revealed a strong peak at 812 nm, indicating its NIR light-adsorbing ability for effective photothermal conversion upon 808 nm laser irradiation (Fig. 1D). To verify it, the photothermal conversion of GNR at different GNR concentrations and different NIR powers were investigated. As shown in Fig. 1E, GNR exhibited desired photothermal conversion efficiency, which was concentration-dependent, and at GNR concentration of 100 μg/mL, the temperature was rapidly increased by 25.1 °C within 4 min of NIR irradiation at the power of 2.0 W/cm^2. The photothermal conversion of GNR was also NIR laser power-dependent. At the power of 0.5 W/cm^2 and GNR concentration of 100 μg/mL, the

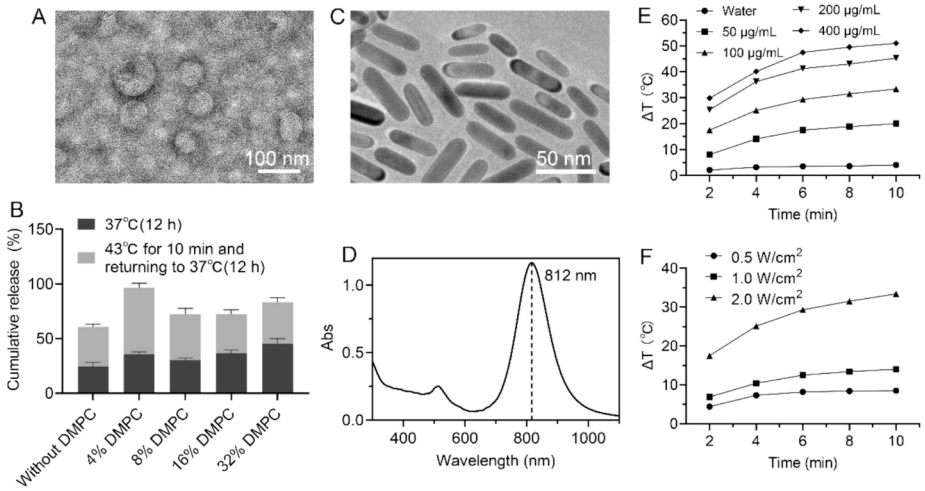

Fig. 1. Characterization of TSL and GNR. (A) Representative TEM image of TSL formulated with 63 % DPPC, 4 % DMPC, 30 % Chol, and 3 % DSPE-PEG-SH. (B) Cumulative DOX release profiles of TSL with or without DMPC under PTT treatment condition (37 °C for 12 h plus 43 °C for 10 min and returning to 37 °C for another 12 h, 24 h in total). (C) TEM image and (D) UV–vis spectrum of GNR. (E) Photothermal conversion efficiency of GNR at different concentrations (50, 100, 200, and 400 μg/mL) under NIR laser irradiation (2.0 W/cm^2). (F) Photothermal conversion efficiency of GNR (100 μg/mL) irradiated by NIR laser of different powers (0.5, 1.0, and 2.0 W/cm^2). Data were expressed at mean ± SD ($n = 3$).

temperature could be increased by 7.3 °C within 4 min (Fig. 1F). Thereby, this safer NIR power was chosen for cell and animal experiments.

3.2. PTT significantly potentiates in vitro anti-tumor outcome of the nanoplatform

In the following, MTT was performed to study the cytotoxicity of GNR, DOX, DOX-TSL, and the nanoplatform of DOX-TSL and GNR against RM-1 cells. As revealed in Fig. 2A, the cytotoxicity of GNR was concentration-dependent, which could be to some extent boosted upon NIR irradiation at the power of 0.5 W/cm^2. At the concentration of 100 μg/mL, the cell survival rate was nearly 90 %; together with its good photothermal conversion and less temperature increment to mild hyperthermia (~43 °C) for improved safety when irradiating (Fig. 1F) (Gao et al., 2022), this relatively biocompatible concentration was used for NIR irradiation in further cell experiments. On the other hand, the cytotoxicity of DOX was far higher than that of GNR, which was also concentration-dependent. Moreover, mild-hyperthermia PTT alone did not exert significant cytotoxicity to the cells and could, however, significantly enhanced the cytotoxicity of DOX (DOX + GNR + NIR *vs* DOX) (Fig. 2B), which was consistent with the literature that PTT could sensitize tumor cells to therapies (Tang et al., 2024). Compared with DOX, the cytotoxicity of DOX-TSL was significantly inhibited and was dramatically magnified when being combined with PTT (DOX-TSL + GNR + NIR *vs* DOX-TSL), resulting from PTT and its triggered thermo-sensitive release for boosted chemotherapy. Moreover, it was observed that PTT magnified the cytotoxicity of DOX-TSL more than DOX (DOX-TSL + GNR + NIR *vs* DOX + GNR + NIR), indicating that DOX-TSL promoted DOX uptake through nanoparticle-mediated endocytosis. These internalized DOX was shielded by TSL, leading to weak fluorescence as well as reduced cytotoxicity of DOX-TSL in comparison to free DOX, and was however, released for strong fluorescence and enhanced anti-tumor outcome upon PTT (Fig. 2C and D). This result was also consistent with the release profiles that TSL containing 4 % DMPC kept stable under the physiological condition but was capable of sensitively responding to mild hyperthermia (Fig. 1B and Table S2). Moreover, it was noted that in MTT assay, the difference between DOX + GNR + NIR and DOX-TSL + GNR + NIR became marginal over increased DOX concentration, because the cytotoxicity of DOX was approaching the plateau.

Enhanced *in vitro* anti-tumor outcome of the nanoplatform combined with PTT was further corroborated by Calcein-AM/PI double staining and cell migration assay. Living/dead cell staining revealed that almost all cells were living in control group and a small number of dead cells stained by red were observed after the treatment with DOX. Especially,

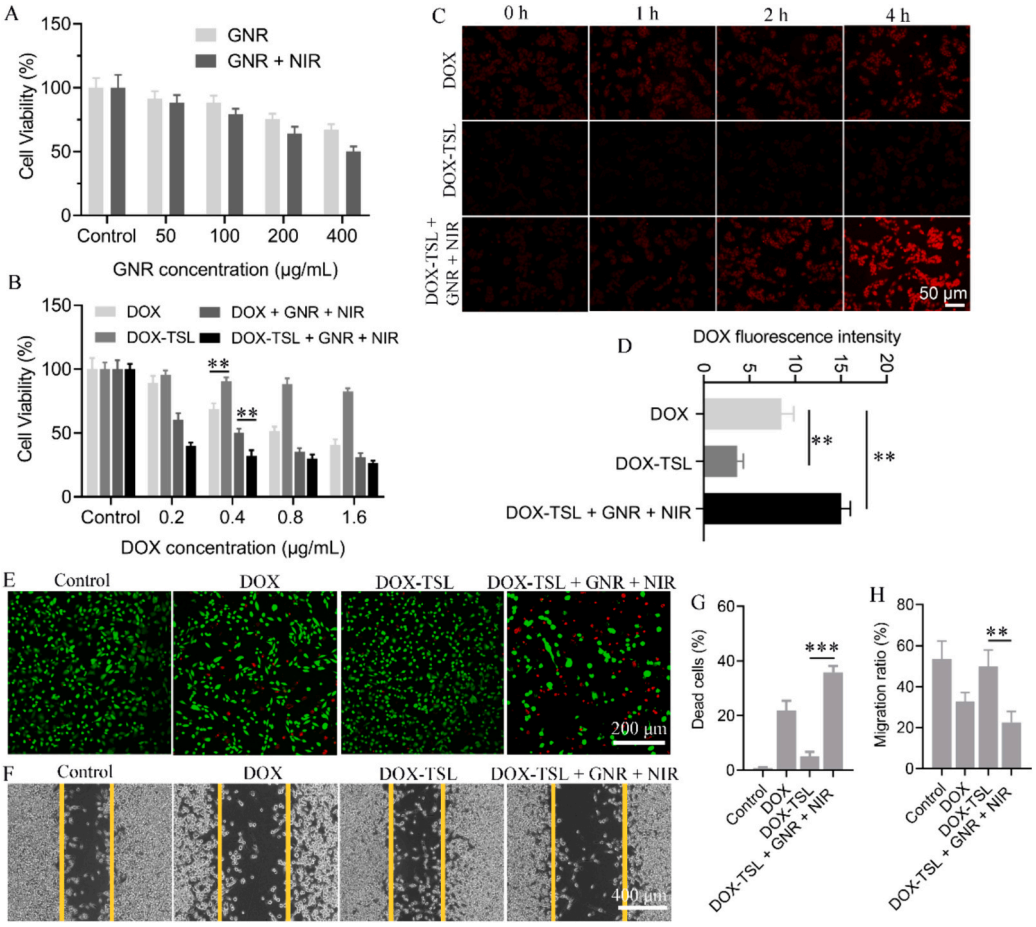

Fig. 2. PTT-combined thermo-sensitive release for improved *in vitro* anti-tumor outcome. (A) MTT assay of GNR with or without NIR irradiation. GNR concentrations varied from 50 to 400 μg/mL. (B) MTT assay of DOX, DOX-TSL, the nanoplatform of DOX-TSL and GNR with or without NIR irradiation. DOX concentrations varied from 0.2 to 1.6 μg/mL, while GNR concentration was fixed at 100 μg/mL. (C) Intracellular DOX release of DOX, DOX-TSL, and the nanoplatform with or without NIR irradiation (D) corresponding quantitative analysis of DOX fluorescence intensity. (E) Calcein-AM/PI double staining of RM-1 cells and (G) corresponding quantitative analysis of dead cells after the treatment with DOX, DOX-TSL, and the nanoplatform with or without NIR irradiation. DOX and GNR concentrations were 0.4 and 100 μg/mL, respectively. (F) Wound-healing assay of RM-1 cells and (H) corresponding quantitative analysis of migration ratio after the treatment with DOX, DOX-TSL, and the nanoplatform with NIR irradiation. DOX and GNR concentrations were 0.4 and 100 μg/mL, respectively. Data were expressed at mean ± SD ($n = 6$ for A and B; $n = 3$ for D, G, and H). $^{**}p < 0.01$ and $^{***}p < 0.001$.

compared with DOX-TSL group with barely observed dead cells, the nanoplatform upon NIR irradiation significantly induced cell death (Fig. 2E and G). Similar trend was found in cell migration assay (Fig. 2F and H). The results of MTT, living/dead cell staining, and wound healing were in good consistence.

3.3. *Improved drug delivery of the nanoplatform in combination with PTT effectively inhibits bone metastasis and relieves CIBP*

DOX and GNR contents in various tissues of tumor-bearing mice were determined through HPLC and ICP-OES, respectively, to study the tissue distribution of the nanoplatform. As shown in Fig. 3A, following intravenous injection, DOX in different formulations was widely distributed in the heart, liver, spleen, lung, kidney, tumor-free bone, and tumor-bearing bone. Especially, DOX-TSL and the nanoplatform showed a relatively high DOX distribution compared with free DOX, corroborating the fact that nanomedicines could effectively improve pharmacokinetics of free drugs to facilitate drug delivery (Karahmet Sher et al., 2024; Shen et al., 2024). GNR in the nanoplatform displayed similar tissue distribution to DOX-TSL (Fig. 3B), indicating that GNR was simultaneously delivered by DOX-TSL through its coupling with TSL mediated by gold-thiol affinity. It was worthy of noting that DOX as well as GNR distribution of the nanoplatform determined by HPLC and ICP-OES, respectively, was total content, which could not reflect thermo-sensitive release state. Therefore, NIR fluorescence imaging was carried out to evaluate sensitive release. As the luminescence of DOX is out of NIR window, which can be greatly interfered by background autofluorescence when being used for *in vivo* fluorescence imaging (Liu et al., 2023b), the main tissues were harvested for *ex vivo* imaging immediately after NIR irradiation. The results demonstrated that without NIR irradiation, DOX fluorescence of the nanoplatform in various tissues was weak with a relatively strong fluorescence observed in the liver. Upon local NIR irradiation, DOX fluorescence in tumor-bearing bone was significantly enhanced, because of DOX release for direct observation of its fluorescence (Fig. 3C and D). The results also suggested that local NIR irradiation at bone metastatic site did not trigger DOX release in the other tissues, indicating its safety.

Therapeutic outcome in pronging survival and relieving CIBP was investigated with the protocol illustrated in Fig. 4A. The result showed that the mean survival time of PBS, DOX, DOX-TSL, and DOX-TSL + GNR + NIR groups was 20.5, 20, 22, and 30 days, respectively (Fig. 4B). Single chemotherapy of DOX had no any beneficial effects on survival. Only marginal improvement was observed in DOX-TSL group, indicating the inability of conventional NDDSs in treating bone metastasis. GNR-assisted PTT boosted chemotherapy of DOX-TSL for significantly improving survival time. Aside from poor survival time and rate, one of other key fears associated with bone metastasis is CIBP (Yang et al., 2024). As shown in Fig. 4C and D, bone metastasis caused severe CIBP, showing significantly decreased paw withdrawal threshold and withdrawal latency (without treatment *vs* baseline). CIBP was potentiated over time (PBS *vs* without treatment), suggesting that the progression of bone metastasis could further aggravate CIBP. DOX-TSL as well as DOX treatment was unable to relieve CIPB; in contrast, the nanoplatform upon NIR irradiation effectively relieved CIPB (DOX-TSL + GNR + NIR *vs* DOX-TSL). Moreover, it was observed that compared with without treatment group, the paw withdrawal threshold and withdrawal latency was significantly elevated. This result might indicate that the progression of bone metastasis is inhibited rather than delayed in this case.

On the 20th day after tumor modeling, clinical X-ray and CT imaging were performed to investigate bone situation. Bone metastasis would

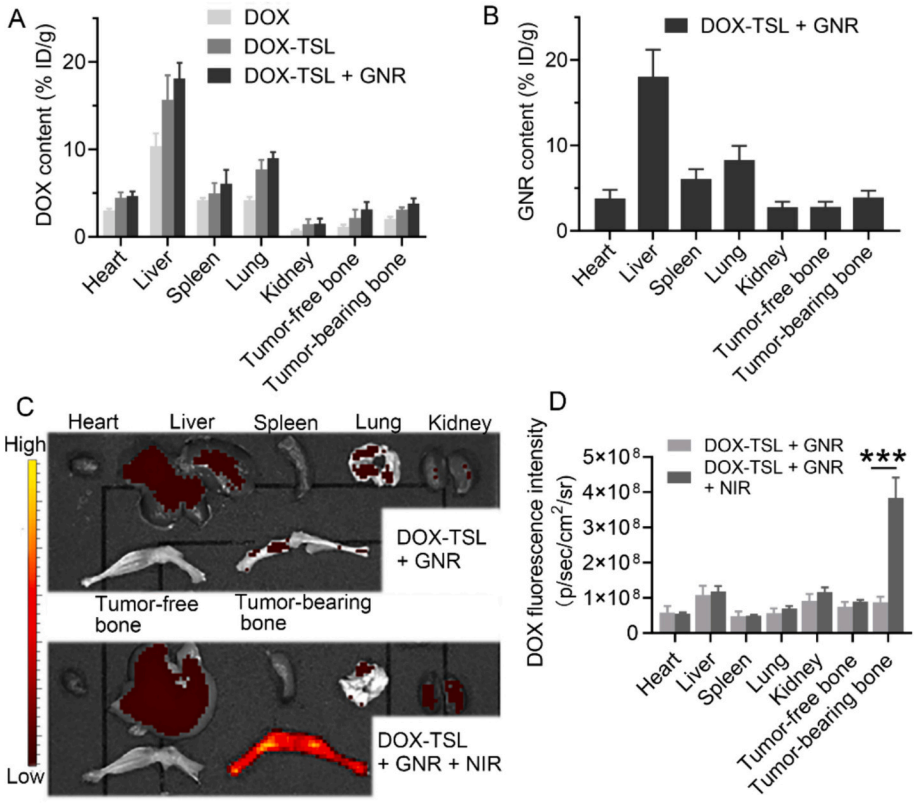

Fig. 3. Tissue biodistribution and thermo-sensitive DOX release upon NIR irradiation. (A) DTX and (B) GNR contents of different drug formulations in the heart, liver, spleen, lung, kidneys, heart, tumor-free bone, and tumor-bearing bone at 12 h post-injection. (C) DOX fluorescence imaging of harvested tissues immediately after NIR irradiation and (D) corresponding quantitative analysis. Tumor-bearing mice received intravenous treatment at 5 mg/kg body weight of DOX and 10 mg/kg body weight of GNR. In the case of NIR irradiation, bone metastatic site of mice was irradiated for 10 min at the power of 0.5 W/cm^2 at 12 h post-injection. Data are expressed as mean ± SEM ($n = 3$). ***$p < 0.001$.

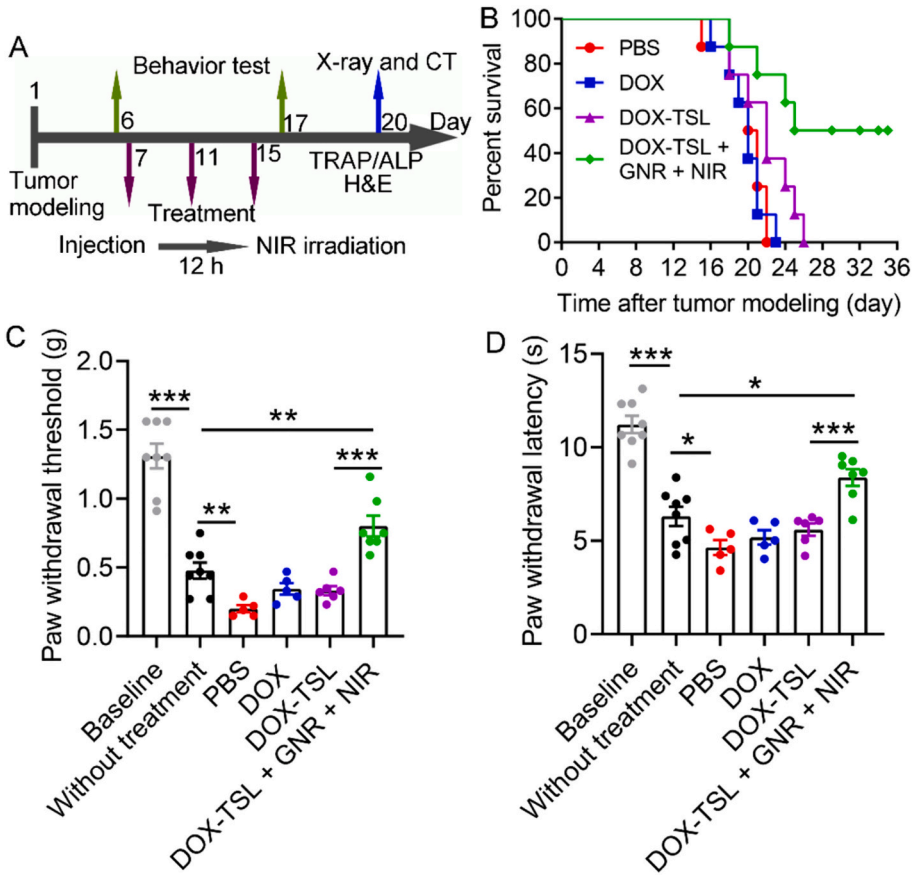

Fig. 4. *In vivo* therapeutic outcome in pronging survival and relieving CIBP. (A) Protocol of drug treatment for *in vivo* therapeutic evaluation. Tumor-bearing mice received intravenous injection at 7th, 11st, and 15th days at 5 mg/kg body weight of DOX and 10 mg/kg body weight of GNR. At 12 h post-injection, bone metastatic site of mice was irradiated for 10 min at the power of 0.5 W/cm^2. (B) Survival situation monitoring. (C) Paw withdrawal threshold and (D) paw withdrawal latency of mice before and after drug treatment. Data of baseline group came from random 8 mice before tumor modeling, while data of without treatment group were acquired from random 8 tumor-bearing mice at 6th day after tumor modeling, prior to grouping for drug treatment. Data are presented as mean ± SEM ($n = 8$). *$p < 0.05$, **$p < 0.01$, and ***$p < 0.001$.

alter the functions of osteoblasts and osteoclasts, resulting in bone destruction (Mao et al., 2023), as verified by our results. As shown in Fig. 5A and B, compared with contralateral tumor-free bone with well-defined bone morphology and structure, tumor-bearing bone displayed severe bone fracture, loss, and hyperplasia, which invaded peripheral tissue. This result also suggests that bone metastasis from prostate cancer is both osteoblastic and osteolytic, of which osteolysis might be dominated (Loots and Guise, 2024). Like free DOX, the therapeutic outcome of conventional DOX-TSL was unsatisfactory with slightly inhibited bone destruction observed in these two groups. Comparatively, bone morphology and structure were largely preserved in DOX-TSL + GNR + NIR, although soft tissue around bone metastasis was still somewhat swelling, which was probably caused by bone metastasis-induced inflammation. The results of X-ray and CT imaging were consistent. Afterwards, the mice were sacrificed and tumor-bearing bone as well as tumor-free bone was harvested and decalcified for H&E and TRAP/ALP staining for histopathological comparison. H&E demonstrated that tumor-free bone was characteristic of normal trabecular bone and normal bone marrow containing massive bone marrow cells, while rapidly proliferating tumor cells destroyed trabecular bone, almost filling the whole bone marrow, once bearing tumor (Fig. 5C). Although DOX-TSL as well as DOX treatment could kill tumor cells and preserve trabecular bone to some extent, tumor cells still occupied the majority of the bone marrow. In contrast, after the treatment with DOX-TSL + GNR + NIR, the bone became histologically similar to tumor-free bone, indicating that bone metastasis was efficaciously inhibited. TRAP/ALP staining was further carried out to detect the activities of osteoclasts and osteoblasts. It is reported that there is a dynamic balance between osteoclasts and osteoblasts in healthy bone and herein, TRAP/ALP staining of tumor-free bone suggested that the activity of osteoclasts stained by wine red should play a predominant role in this balance (Fig. 5D). Unexpectedly, while the activity of osteoblasts stained as dark brown was increasing, osteoclasts seemed to disappear in PBS group. The increase of the activity of osteoblasts for bone formation to compensate bone loss caused by tumor might contribute to such a phenomenon (Chen et al., 2023). The activity of osteoclasts slightly increased after the treatment with DOX-TSL and DOX, which remarkably increased to achieve a rebalance with the activity of osteoblasts after the treatment with DOX-TSL + GNR + NIR. Generally, it was a corollary that thermo-sensitive chemotherapy of DOX-TSL in combination with GNR-assisted local PTT could effectively kill tumor cells in the bone, thus rebalancing the turnover of osteoclasts and osteoblasts for relieving CIBP and prolonging survival.

Meanwhile, some main tissue, such as the heart, liver, spleen, lung, and kidney were also harvested for H&E staining and no toxicity was observed in all groups. H&E staining also revealed distant metastasis from bone to the lung, which was significantly inhibited after the treatment with DOX-TSL + GNR + NIR (Fig. S3).

4. Conclusion

In summary, we try to utilize a simple nanoplatform composed of TSL as carrier of DOX and GNR as photothermal agent to treat bone metastasis through improved chemotherapy combined with PTT. The

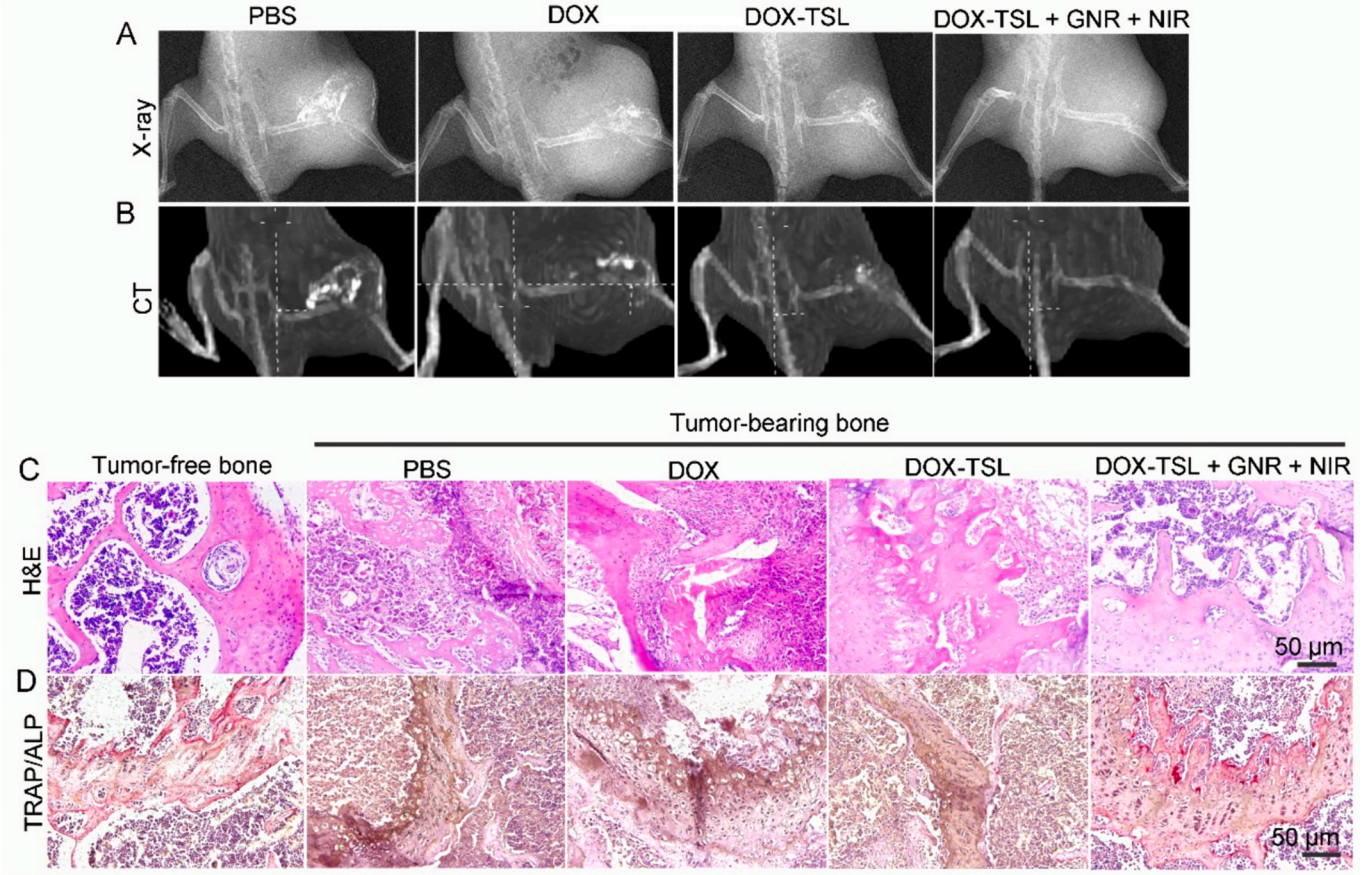

Fig. 5. Bone histological evaluation. (A) Whole-body X-ray and (B) CT imaging of tumor-bearing mice. (C) H&E and (D) TRAP/ALP staining of harvested tumor-bearing bone as well as tumor-free bone. Osteoclasts and osteoblasts were stained as wine red and dark brown, respectively, in TRAP/ALP staining, respectively. (For interpretation of the references to colour in this figure legend, the reader is referred to the web version of this article.)

synthesized TSL showed a high stability to maintain its payload under physiological condition and a high sensitivity to mild hyperthermia for rapid release, while GNR displayed a desired photothermal conversion capacity upon 808 nm NIR irradiation. The pre-synthesized DOX-TSL and GNR were incubated and the nanoplatform was obtained through gold-thiol coupling between GNR and TSL. Cell experiments revealed that upon NIR irradiation, the therapeutic outcome of the nanoplatform was significantly improved through the anti-tumor outcome of PTT itself, PTT-triggered thermo-sensitive DOX release, and PTT-augmented sensitivity of tumor cells to DOX. Animal experiments demonstrated that the nanoplatform facilitated simultaneous delivery of DOX and GNR to target site; through local NIR irradiation, the nanoplatform efficaciously killed tumor cells in the bone and thus rebalanced the turnover of osteoclasts and osteoblasts, which ultimately prolonged survival time and relieved CIBP. The combination of TSL and GNR thus emerges as easy-to-operate but effective nanoplatform to treat bone metastasis.

CRediT authorship contribution statement

Jia Gu: Writing – original draft, Methodology, Investigation, Formal analysis. **Lifan Jiang:** Validation, Investigation, Formal analysis. **Zhongping Chen:** Writing – original draft, Validation, Methodology, Investigation. **Jun Qi:** Writing – review & editing, Validation, Supervision, Methodology, Funding acquisition, Conceptualization.

Declaration of competing interest

The authors declare that they have no known competing financial interests.

Data availability

Data will be made available on request.

Acknowledgments

This study was supported by grants from Jiangsu Provincial Research Hospital (YJXYY202204-YSB42).

Appendix A. Supplementary data

Supplementary data to this article can be found online at https://doi.org/10.1016/j.ijpx.2024.100282.

References

Amiryaghoubi, N., Fathi, M., Barar, J., Omidian, H., Omidi, Y., 2023. Advanced nanoscale drug delivery systems for bone cancer therapy. BBA-Mol. Basis Dis. 1869, 166739.

Ashique, S., Faiyazuddin, M., Afzal, O., Gowri, S., Hussain, A., Mishra, N., Garg, A., Maqsood, S., Akhtar, M.S., Altamimi, A.S., 2023. Advanced nanoparticles, the hallmark of targeted drug delivery for osteosarcoma-an updated review. J. Drug Deliv. Sci. Technol. 87, 104753.

Cao, M., Long, M., Chen, Q., Lu, Y., Luo, Q., Zhao, Y., Lu, A., Ge, C., Zhu, L., Chen, Z., 2019. Development of β-elemene and Cisplatin Co-Loaded Liposomes for Effective Lung Cancer Therapy and Evaluation in Patient-Derived Tumor Xenografts. Pharm. Res. 36, 121.

Chao, B., Jiao, J., Yang, L., Wang, Y., Jiang, W., Yu, T., Wang, L., Liu, H., Zhang, H., Wang, Z., Wu, M., 2023. Application of advanced biomaterials in photothermal therapy for malignant bone tumors. Biomater. Res. 27, 116.

Chen, Z.-H., Wu, J.-J., Guo, D.-Y., Li, Y.-Y., Chen, M.-N., Zhang, Z.-Y., Yuan, Z.-D., Zhang, K.-W., Chen, W.-W., Tian, F., Ye, J.-X., Li, X., Yuan, F.-L., 2023. Physiological

functions of podosomes: from structure and function to therapy implications in osteoclast biology of bone resorption. Ageing Res. Rev. 85, 101842.
Chen, H., Xu, J., Sun, J., Jiang, Y., Zheng, W., Hu, W., Qian, H., 2024. Recent advances on thermosensitive hydrogels-mediated precision therapy. Asian J. Pharm. Sci. 19, 100911.
Dixon, W.J., 1980. Efficient analysis of experimental observations. Annu. Rev. Pharmacol. Toxicol. 20, 441–462.
Fan, Z., Iqbal, H., Ni, J., Khan, N.U., Irshad, S., Razzaq, A., Alfaifi, M.Y., Elbehairi, S.E.I., Shati, A.A., Zhou, J., Cheng, H., 2024. Rationalized landscape on protein-based cancer nanomedicine: recent progress and challenges. Int. J. Pharm. X 7, 100238.
Gao, X., Li, L., Cai, X., Huang, Q., Xiao, J., Cheng, Y., 2021. Targeting nanoparticles for diagnosis and therapy of bone tumors: Opportunities and challenges. Biomaterials 265, 120404.
Gao, P., Wang, H., Cheng, Y., 2022. Strategies for efficient photothermal therapy at mild temperatures: Progresses and challenges. Chin. Chem. Lett. 33, 575–586.
Gautam, R., Matai, I., Soni, S., 2024. Photothermally modulated drug release kinetics for pH and thermo-responsive hydrogel system. J. Mater. Res. 39, 398–411.
Guo, B., Sheng, Z., Hu, D., Liu, C., Zheng, H., Liu, B., 2018. Through Scalp and Skull NIR-II Photothermal Therapy of Deep Orthotopic Brain Tumors with Precise Photoacoustic Imaging Guidance. Adv. Mater. 30, 1802591.
Hargreaves, K., Dubner, R., Brown, F., Flores, C., Joris, J., 1988. A new and sensitive method for measuring thermal nociception in cutaneous hyperalgesia. Pain 32, 77–88.
Hu, B., Zhang, Y., Zhang, G., Li, Z., Jing, Y., Yao, J., Sun, S., 2022. Research progress of bone-targeted drug delivery system on metastatic bone tumors. J. Control. Release 350, 377–388.
Huang, X., Ding, Y., Gu, J., Tao, Y., Wu, X., Luo, Q., Li, Y., Cai, X., Chen, Z., 2024. Organ-selective lipid nanoparticles for precise cancer therapy: beyond liposomes and polymeric micelles. Chem. Eng. J. 494, 153171.
Karahmet Sher, E., Alebić, M., Marković Boras, M., Boškailo, E., Karahmet Farhat, E., Karahmet, A., Pavlovic, B., Sher, F., Lekic, L., 2024. Nanotechnology in Medicine Revolutionizing Drug Delivery for cancer and Viral Infection Treatments. Int. J. Pharm, p. 124345.
Lavrador, P., Gaspar, V.M., Mano, J.F., 2018. Stimuli-responsive nanocarriers for delivery of bone therapeutics - Barriers and progresses. J. Control. Release 273, 51–67.
Li, M., Yu, B., Wang, S., Zhou, F., Cui, J., Su, J., 2023. Microenvironment-responsive nanocarriers for targeted bone disease therapy. Nano Today 50, 101838.
Li, S., Kang, Y., Zeng, Y., 2024. Targeting tumor and bone microenvironment: Novel therapeutic opportunities for castration-resistant prostate cancer patients with bone metastasis. BBA-Rev. Cancer 1879, 189033.
Liu, L., Guo, Z., Xu, L., Xu, R., Lu, X., 2011. Facile purification of colloidal NIR-responsive gold nanorods using ions assisted self-assembly. Nanoscale Res. Lett. 6, 143.
Liu, S., Wang, Z., Wei, Q., Duan, X., Liu, Y., Wu, M., Ding, J., 2023a. Biomaterials-enhanced bioactive agents to efficiently block spinal metastases of cancers. J. Control. Release 363, 721–732.
Liu, X.M., Sun, J.J., Gu, J., Weng, L.Y., Wang, X.T., Zhu, L., Luo, Q.Q., Chen, Z.P., 2023b. Effective drug and shRNA delivery for synergistic treatment of triple-negative breast cancer by sequentially targeting tumor hypoxia. Chem. Eng. J. 470, 144271.
Long, M.M., Lu, A.L., Lu, M., Weng, L.Y., Chen, Q.P., Zhu, L., Chen, Z.P., 2020. Azo-inserted responsive hybrid liposomes for hypoxia-specific drug delivery. Acta Biomater. 115, 343–357.
Long, M.M., Liu, X.M., Huang, X.L., Lu, M., Wu, X.M., Weng, L.Y., Chen, Q.P., Wang, X. T., Zhu, L., Chen, Z.P., 2021. Alendronate-functionalized hypoxia-responsive polymeric micelles for targeted therapy of bone metastatic prostate cancer. J. Control. Release 334, 303–317.
Loots, G.G., Guise, T.A., 2024. Mechanisms underlying Osteolytic and Osteoblastic Bone Metastases. In: Randall, R.L. (Ed.), Metastatic Bone Disease: An Integrated Approach to Patient Care. Springer International Publishing, Cham, pp. 17–35.
Lorange, J.-P., Ramirez Garcia Luna, J., Grou-Boileau, F., Rosenzweig, D., Weber, M.H., Akoury, E., 2023. Management of bone metastasis with zoledronic acid: a systematic review and Bayesian network meta-analysis. J. Bone Oncol. 39, 100470.
Mao, L., Wang, L., Xu, J., Zou, J., 2023. The role of integrin family in bone metabolism and tumor bone metastasis. Cell Death Dis. 9, 119.
Ren, X., Chen, X., Geng, Z., Su, J., 2022. Bone-targeted biomaterials: strategies and applications. Chem. Eng. J. 446, 137133.
Roodman, G.D., 2004. Mechanisms of Bone Metastasis. N. Engl. J. Med. 350, 1655–1664.
Roy, S., Bag, N., Bardhan, S., Hasan, I., Guo, B., 2023. Recent progress in NIR-II fluorescence imaging-guided drug delivery for cancer theranostics. Adv. Drug Deliv. Rev. 197, 114821.
Shen, X., Sheng, H., Zhang, Y., Dong, X., Kou, L., Yao, Q., Zhao, X., 2024. Nanomedicine-based disulfiram and metal ion co-delivery strategies for cancer treatment. Int. J. Pharm. X 7, 100248.
Sheng, P., Bu, C., Hui, T., Zhou, L., Chen, H., Zhou, G., 2023. Polydopamine-activated celastrol carbon dots for synergistic chemotherapy-photothermal therapy of tumors. Int. J. Pharm. X 6, 100218.
Svensson, E., Christiansen, C.F., Ulrichsen, S.P., Rørth, M.R., Sørensen, H.T., 2017. Survival after bone metastasis by primary cancer type: a Danish population-based cohort study. BMJ Open 7, e016022.
Tang, F., Ding, A., Xu, Y., Ye, Y., Li, L., Xie, R., Huang, W., 2024. Gene and Photothermal Combination Therapy: Principle, Materials, and Amplified Anticancer intervention. Small 20, 2307078.
Tao, Y., Chen, Z., 2024. Hypobaric hypoxia exposure regulates tissue distribution of nanomedicine for enhanced cancer therapy. Cancer Nanotechnol. 15, 21.
Taylor, M.L., Wilson Jr., R.E., Amrhein, K.D., Huang, X., 2022. Gold nanorod-assisted photothermal therapy and improvement strategies. Bioengineering 9, 200.
Thapa, R.K., Kim, J.O., 2023. Nanomedicine-based commercial formulations: current developments and future prospects. J. Pharm. Investig. 53, 19–33.
Wang, F.F., Chen, L., Zhang, R., Chen, Z.P., Zhu, L., 2014. RGD peptide conjugated liposomal drug delivery system for enhance therapeutic efficacy in treating bone metastasis from prostate cancer. J. Control. Release 196, 222–233.
Weilbaecher, K.N., Guise, T.A., McCauley, L.K., 2011. Cancer to bone: a fatal attraction. Nat. Rev. Cancer 11, 411–425.
Yang, Y., Yang, W., Zhang, R., Wang, Y., 2024. Peripheral Mechanism of Cancer-Induced Bone Pain. Neurosci. Bull. 40, 815–830.
Yu, Y., Ollodart, J., Contino, K.F., Shiozawa, Y., 2023. Immunotherapy as a potential treatment approach for currently incurable bone metastasis. J. Bone Miner. Metab. 41, 371–379.
Zhang, Y., Li, Y., Liao, W., Peng, W., Qin, J., Chen, D., Zheng, L., Yan, W., Li, L., Guo, Z., 2021. Citrate-stabilized gold nanorods-directed osteogenic differentiation of multiple cells. Int. J. Nanomedicine 16, 2789–2801.